Spin-3/2 nuclear magnetic resonance: Exact analytical solutions for aligned systems and implications for probing Fe-based superconductors

Jaafar N. Ansari [*]
Department of Physics and Astronomy, George Mason University, Fairfax, Virginia 22030, USA

Karen L. Sauer [†]
Department of Physics and Astronomy, George Mason University, Fairfax, Virginia 22030, USA
and Quantum Science and Engineering Center, George Mason University, Fairfax, Virginia 22030, USA

(Received 9 July 2024; revised 22 November 2024; accepted 26 November 2024; published 16 December 2024)

The nuclear magnetic resonance (NMR) spectrum of spin-3/2 nuclei in a static magnetic field aligned with one of the electric field gradient (EFG) principal axes is developed analytically, based on fictitious spin-1/2 formalism. Compact closed-form expressions for the eigenstates and transitions frequencies, as well as the expectation value of the magnetic moment after resonant excitation, are derived. Emphasis is placed on defining and interpreting the associated Rabi frequencies, as a function of excitation direction and ellipticity. It is found that transitions inherently fall into two subsets, depending on their sensitivity to excitation direction, with the Rabi frequency of one subset directly depending on the asymmetry of the EFG. A natural application is the study of Fe-based superconductors, whose antiferromagnetic ordering at low temperatures leads to a strong intrinsic magnetic field aligned with the EFG principal axes. Zero external-field NMR spectra, from powder samples of two such Fe-based superconductors, $BaFe_2As_2$ and $CaFe_2As_2$, are analyzed and exemplify the simplicity in extracting the internal magnetic field, the quadrupole coupling constant, and the EFG asymmetry parameter, which are important for studying magnetic ordering, structural properties, phase transitions, and NMR dynamics. Results compare favorably to conventional high-field NMR experiments done with the rotation of single crystals. Overall, the physical insights, afforded by the exact and concise expressions, will lead to ready interpretation of spin-3/2 spectra as well as precipitating new experimental directions.

DOI: 10.1103/PhysRevB.110.214422

I. INTRODUCTION

Nuclei with spin greater than 1/2 have both a magnetic and an electric quadrupole moment. The former couples to a magnetic field, the latter to an electric field gradient (EFG). Such nuclei can then serve as an internal probe of both magnetic and electric phenomena, and they are addressable using the magnetic dipole's interaction with a radiofrequency excitation, i.e., nuclear magnetic resonance (NMR). Conventionally, experiments are often performed in two limits: (i) in a large magnetic field which is commonly known as high-field NMR, and (ii) in the absence of a magnetic field, often referred to as nuclear quadrupole resonance (NQR). In this paper, we are concerned with the exact NMR theory of spin-3/2 nuclei in the presence of a magnetic field which is aligned with one of the EFG principal axes. The full continuum of results between the zero-field and high-field limits is addressed.

We tackle this problem using the spin-1/2 formalism, which has not been done before. Although the solution for this system is somewhat involved because the quadrupolar and Zeeman Hamiltonians do not commute, it has been solved exactly for arbitrary field directions [1–4] and by perturbation theory many times over using a variety of techniques [5,6]. In addition, software has been written that simulates such spectra [7,8]. Previous work tackling the full solution is useful for computational analysis and modeling, however they lack physical insight and the ability to be used for straightforward data analysis. With this in mind, a set of tractable analytical expressions in the EFG-aligned case is notably missing and would elevate the quality of both the quantitative and qualitative analysis of these systems.

The present work addresses this problem, with the aim of going beyond just the eigenfrequencies, eigenstates, and transition rates, by deriving explicit expressions for the oscillating nuclear magnetization, including its direction, produced after a pulse of resonant radiofrequency excitation. The Rabi frequency, dictating the efficacy of the excitation, is proportional to the radiofrequency strength, as well as a modifying geometric term. This geometric term λ depends on the direction of the excitation field as well as the relative strengths of the static field components. An excitation pattern, specific to the transition frequency, can therefore be visualized through λ. Such visualization has only been done in the pure NQR case [9]. Select transitions directly depend on the asymmetry of the electric field gradient with respect to the static magnetic field. The use of the Rabi frequency for EFG determination, including asymmetry, has been studied in the case of pure NQR through the use of nutation spectroscopy [10,11].

[*]Contact author: jansari@gmu.edu
[†]Contact author: ksauer1@gmu.edu

Computational results of nutation spectroscopy in the presence of a magnetic field have also been performed [12,13], but they lack analytical expressions. This paper remedies this by presenting exact expressions of the Rabi frequencies for the case of EFG alignment with the magnetic field.

We take the Fe-based superconductors (FeSCs) as an example, and we apply our expressions to demonstrate how they can be used for analysis. These unconventional high-T_c superconductors are perfectly suited for the type of analysis described in this paper since they have spin-3/2 nuclei which experience a large ∼1 T internally supplied magnetic field from the antiferromagnetic ordering of Fe magnetic moments. The orthorhombic/tetragonal crystal symmetry dictates that the field is always oriented along one of the EFG principal axes [14,15]. Therefore, zero external-field NMR (ZNMR) and a powder sample can be used since both the field and EFG are tied to the crystal symmetry. Detailed analysis of these ZNMR spectra has been limited due to the lack of such expressions that we bring to light in this paper. These materials are of immediate interest in superconductivity research and the broader condensed-matter field, because of the interplay of magnetic and electrical order [16], as well as controversies surrounding the superconductivity mechanism. Some high-T_c oxides also exhibit EFG-aligned hyperfine fields on spin-3/2 nuclei [17,18], and they can be easily studied using the tools introduced in this paper. Other applications can be found in vapor cells [19] and other antiferromagnetic materials [20,21].

So, in this paper, we add to the body of knowledge on spin-3/2 particles in magnetic fields by studying the case of the field oriented along one of the EFG principal axes. The paper is organized as follows. In the Theory section, we start by using the fictitious spin-1/2 formalism to derive easy-to-use analytical expressions of the eigenenergies, eigenfrequencies, and eigenstates, along with the matrix elements of the spin angular momentum operators. Formulas for the expectation value of the nuclear magnetic moment and the Rabi frequencies are also presented. The Results section is split into three subsections: (i) the predicted Zeeman-quadrupolar spectrum is visualized, and two case studies of existing FeSC ZNMR data are examined to demonstrate the analysis using the derived expressions; (ii) the full solution of the continuum, that is, for all possible magnetic field and EFG strengths is shown; and (iii) the geometric behavior of the Rabi frequencies is discussed.

II. THEORY

An electrically quadrupolar nucleus that has a quadrupole moment Q and a nuclear magnetic moment, in the presence of an EFG and a magnetic field, will experience energy level splitting due to both of these interactions. The EFG comes from the local electronic environment and is a tensor defined as $V_{ij} = \partial^2 V/\partial x_i \partial x_j|_{\mathbf{r}_0}$, where V is the electric potential, and it is evaluated at the position of the nucleus $\mathbf{r}_0$. A set of three principal axes can be determined upon diagonalization of the tensor. With one axis of the EFG principal axes assumed to align with the magnetic field in the z-direction, the dominant Hamiltonian is given by the sum of the Zeeman Hamiltonian and the quadrupolar Hamiltonian [22]:

$$H = \hbar\left[I_z\omega_0 + \tfrac{1}{6}\omega_Q\left(3I_z^2 - I^2\right) + \tfrac{1}{12}\omega_\perp(I_+^2 + I_-^2)\right], \quad (1)$$

where $\mathbf{I}$ is the nuclear spin angular momentum operator divided by the reduced Planck constant $\hbar$. The quadrupole coupling constant is defined as

$$\omega_Q = \frac{3eQ}{2I(2I-1)\hbar}V_{zz}, \quad (2)$$

where e is the elementary charge. We define the Zeeman frequency as

$$\omega_0 = -\gamma B_0, \quad (3)$$

where the static magnetic field is denoted by B_0, and γ is the nuclear gyromagnetic ratio. We choose $\hat{z}$ so that $\omega_0 \geqslant 0$; that is, $\hat{z}$ is antiparallel to $\mathbf{B}_0$ for a positive γ, and $\hat{z}$ is parallel to $\mathbf{B}_0$ for a negative γ. Lastly, $\omega_\perp$ is defined so that $\omega_\perp/\omega_Q = (V_{xx} - V_{yy})/V_{zz} \equiv \eta$ (commonly referred to as the EFG asymmetry parameter):

$$\omega_\perp = \frac{3eQ}{2I(2I-1)\hbar}(V_{xx} - V_{yy}). \quad (4)$$

The coordinate system is chosen so that $V_{xx} \geqslant V_{yy}$. Note that η, as a result of this, is unrestricted in its range since V_{zz} is not necessarily the largest EFG component. The sign of ω_Q can be either positive or negative depending on Q and V_{zz}. We find that experimentally observed results, however, are insensitive to the sign of ω_Q. More details are given in the captions of Tables I and II.

Finally, it is useful for the fictitious spin-1/2 formalism to write the Hamiltonian in matrix form in the Zeeman basis with rows and columns rearranged to clearly show two 2×2 subblocks:

$$H = \begin{bmatrix} \frac{3\omega_0+\omega_Q}{2} & \frac{\sqrt{3}\omega_\perp}{6} & 0 & 0 \\ \frac{\sqrt{3}\omega_\perp}{6} & \frac{-\omega_0-\omega_Q}{2} & 0 & 0 \\ 0 & 0 & \frac{\omega_0-\omega_Q}{2} & \frac{\sqrt{3}\omega_\perp}{6} \\ 0 & 0 & \frac{\sqrt{3}\omega_\perp}{6} & \frac{-3\omega_0+\omega_Q}{2} \end{bmatrix}. \quad (5)$$

The new ordering is $|3/2\rangle, |-1/2\rangle, |1/2\rangle, |-3/2\rangle$ of both the rows and the columns.

Diagonalization of the Hamiltonian in Eq. (1) results in the eigenenergies and eigenstates (in the eigenbasis of I_z) as given

TABLE I. Eigenstates and eigenenergies of the combined Zeeman-quadrupolar Hamiltonian given in Eq. (1), with angles and frequencies given in Eqs. (3) and (6)–(8). In the expressions below, it is assumed ω_Q is positive. However, for negative ω_Q, this table remains valid by the simple interchanging of ω_+ and ω_-, and θ_η and θ'_η within the table.

Label	Eigenenergy	Eigenstate
1	$\frac{\hbar}{2}(\omega_0 + \omega_+)$	$\cos\frac{\theta_\eta}{2}\left\|\frac{3}{2}\right\rangle + \sin\frac{\theta_\eta}{2}\left\|\frac{-1}{2}\right\rangle$
2	$\frac{\hbar}{2}(\omega_0 - \omega_+)$	$-\sin\frac{\theta_\eta}{2}\left\|\frac{3}{2}\right\rangle + \cos\frac{\theta_\eta}{2}\left\|\frac{-1}{2}\right\rangle$
1′	$\frac{\hbar}{2}(-\omega_0 + \omega_-)$	$\cos\frac{\theta'_\eta}{2}\left\|\frac{1}{2}\right\rangle + \sin\frac{\theta'_\eta}{2}\left\|\frac{-3}{2}\right\rangle$
2′	$\frac{\hbar}{2}(-\omega_0 - \omega_-)$	$-\sin\frac{\theta'_\eta}{2}\left\|\frac{1}{2}\right\rangle + \cos\frac{\theta'_\eta}{2}\left\|\frac{-3}{2}\right\rangle$

TABLE II. Exact expressions for the six possible transition frequencies and their associated spin angular momentum operator matrix elements. The first four lines of the table are those transitions that are unresponsive to excitations parallel to the magnetic field, labeled as the "O" transitions, and they are given analogous names familiar in the high-field NMR limit. The last two unnamed transitions are unresponsive to excitations orthogonal to the magnetic field, and they are labeled as the "P" transitions. The labeling of the transitions (O vs P) is with respect to maximum responsiveness. The angles and frequencies are given in Eqs. (3) and (6)–(8). In the expressions below, it is assumed ω_Q is positive. However, for negative ω_Q, this table remains valid by the simple interchanging of ω_+ and ω_-, and θ_η and θ'_η within the table. Note that these interchanges do not actually change the transition frequencies or the magnitude of the corresponding transition elements, rather only the "p" and "q" state labels assigned to the transition. Therefore, in the ensuing plots, only the positive case is considered.

$p \leftrightarrow q$	Frequency	$\langle p\|I_+\|q\rangle$	$\langle p\|I_-\|q\rangle$	$\langle p\|I_z\|q\rangle$	Transition name
Orthogonal "O" transitions					
$2 \leftrightarrow 2'$	$\omega_0 - \frac{\omega_+}{2} + \frac{\omega_-}{2}$	$\sqrt{3}\cos\left(\frac{\theta_\eta - \theta'_\eta}{2}\right)$	$-2\cos\frac{\theta_\eta}{2}\sin\frac{\theta'_\eta}{2}$	0	ω_ℓ, lower satellite
$1' \leftrightarrow 2$	$-\omega_0 + \frac{\omega_+}{2} + \frac{\omega_-}{2}$	$2\cos\frac{\theta_\eta}{2}\cos\frac{\theta'_\eta}{2}$	$-\sqrt{3}\sin\left(\frac{\theta_\eta - \theta'_\eta}{2}\right)$	0	ω_c, central
$1 \leftrightarrow 1'$	$\omega_0 + \frac{\omega_+}{2} - \frac{\omega_-}{2}$	$\sqrt{3}\cos\left(\frac{\theta_\eta - \theta'_\eta}{2}\right)$	$2\cos\frac{\theta'_\eta}{2}\sin\frac{\theta_\eta}{2}$	0	ω_u, upper satellite
$1 \leftrightarrow 2'$	$\omega_0 + \frac{\omega_+}{2} + \frac{\omega_-}{2}$	$\sqrt{3}\sin\left(\frac{\theta_\eta - \theta'_\eta}{2}\right)$	$-2\sin\frac{\theta_\eta}{2}\sin\frac{\theta'_\eta}{2}$	0	ω_f, forbidden
Parallel "P" transitions					
$1 \leftrightarrow 2$	ω_+	0	0	$-\sin\theta_\eta$	
$1' \leftrightarrow 2'$	ω_-	0	0	$-\sin\theta'_\eta$	

in Table I (see Compliment B_{IV} of Ref. [23]). As shown in Table I, they are defined in terms of the quantities θ_η, θ'_η, and $\omega_\pm$, which are given by

$$\tan\theta_\eta = \frac{|\omega_\perp|}{\sqrt{3}(2\omega_0 + |\omega_Q|)}, \tag{6}$$

$$\tan\theta'_\eta = \frac{|\omega_\perp|}{\sqrt{3}(2\omega_0 - |\omega_Q|)}, \tag{7}$$

$$\omega_\pm = \sqrt{(2\omega_0 \pm |\omega_Q|)^2 + \frac{\omega_\perp^2}{3}}. \tag{8}$$

The angles are limited such that $0 \leqslant \theta_\eta < \pi/2$ and $0 \leqslant \theta'_\eta < \pi$. A geometric visualization of the angles is given in Fig. 1. Upon inspection, the system can be characterized by just three parameters: ω_+, revealing the net strength of the combined field components; θ_η, a metric of the EFG asymmetry; and the relative ratio of the Zeeman and quadrupole contributions,

$$R = \frac{2\omega_0 - |\omega_Q|}{2\omega_0 + |\omega_Q|}. \tag{9}$$

An energy level diagram calculated from these quantities is shown in Fig. 2.

From these energy levels, six possible transition frequencies can be observed as shown in Fig. 2, and they are given in Table II. The expressions for the eigenfrequencies are in agreement with previous work using low-field perturbation theory and exact expressions in the EFG-aligned case [24]. As discussed in more detail below, the observability of these transitions depends on the radiofrequency excitation direction with respect to the magnetic field. More specifically, four of these transitions are completely unresponsive to excitations parallel to the magnetic field and are labeled as the "O" transitions (for "orthogonal"). The other two transitions are unresponsive to excitations orthogonal to the magnetic field and are labeled as the "P" transitions (for "parallel"). The P-transitions are equal to $\omega_\pm$ defined in Eq. (8).

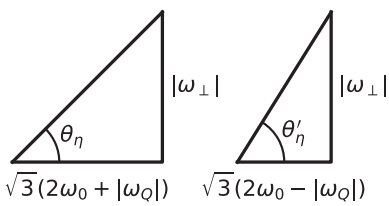

FIG. 1. Visual definitions of θ_η and θ'_η, also defined in Eqs. (6) and (7). These angles can serve as a metric of transverse field asymmetry compared to longitudinal field components.

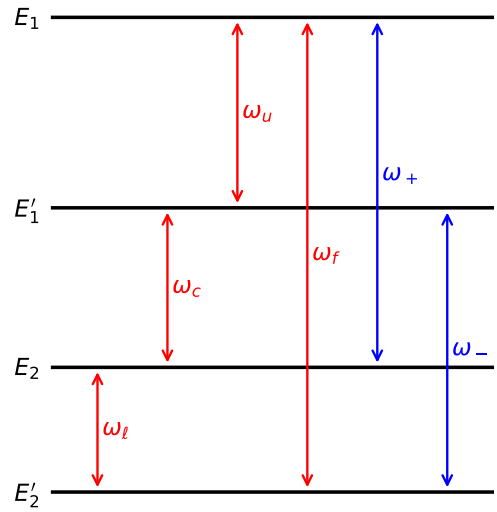

FIG. 2. Energy levels of the combined Zeeman-quadrupolar Hamiltonian. The spacings are drawn to scale, having been calculated for a system with $R = 0.81$ and $\theta_\eta = 0.1$. The transition frequencies are also labeled and defined in Table II. The O-transitions are shown in red, and the P-transitions in blue, also defined in Table II.

TABLE III. Extracted parameters of $BaFe_2As_2$ and $CaFe_2As_2$. Rows with an asterisk were determined by solving the frequency equations from Table II with the fitted peaks from Fig. 4 for the three parameters; otherwise they are quoted directly from the literature. Values without uncertainties were either extracted from a plot or were not given with uncertainties in the original literature. We use the standard notation: ν_Q is the quadrupole coupling constant, H_{int} is the internal magnetic field, and η is the EFG asymmetry parameter defined by $|V_{aa} - V_{bb}|/|V_{cc}|$, where a, b, and c are the lattice parameters of the crystal structure. SC refers to "single crystal" and H is an externally applied magnetic field.

Material	ν_Q (MHz)	H_{int} (T)	η	Methodology	Temperature (K)
$CaFe_2As_2$ [27]	12.4	2.6(1)		NMR SC $H\|\|c$	20
$CaFe_2As_2$ [26]*	11.4(1)	2.59(1)	0.0(1)	ZNMR powder	5
$CaFe_2As_2$ [28]			0.39(5)	NMR SC rotation	20
$CaFe_2As_2$ [29]	12.38(4)	2.63(1)		NMR SC $H\|\|c$	4
$CaFe_2As_2$ [30]	12.9	2.64(5)		NMR SC $H\|\|c$	4.3
$BaFe_2As_2$ [31]	2.21	1.46	1.18	NMR SC rotation	7
$BaFe_2As_2$ [25]*	2.09(3)	1.377(4)	2.0(2)	ZNMR powder	1.5

A measurement is performed by sending a time-dependent perturbation, a radiofrequency pulse with frequency ω resonant with one of the six transitions,

$$H_1 = \hbar\omega_1 \mathbf{I}\cdot\hat{n}\cos(\omega t), \tag{10}$$

where $\omega_1 = -\gamma B_1$ is the Rabi frequency and B_1 is the amplitude of the signal. The excitation direction is $\hat{n} = \sin\theta\cos\varphi\hat{x} + \sin\theta\sin\varphi\hat{y} + \cos\theta\hat{z}$, where φ and θ are the usual azimuth and polar angles with respect to $\mathbf{B}_0$. The response is a net nuclear magnetic moment. For a transition from p to q, its expectation value can be calculated using the fictitious spin-1/2 formalism (see Compliment C_{IV} of Ref. [23]) and is given by

$$\langle\boldsymbol{\mu}\rangle_{pq} = -i\gamma\hbar f_{pq}\sin(\lambda_{pq}\Theta)\langle p|\mathbf{I}|q\rangle e^{i(\omega_{pq}t-\xi_{pq})} + \text{c.c.}, \tag{11}$$

where c.c. stands for the complex conjugate of the preceding term, $f_{pq} = \hbar\omega_{pq}/[2(2I+1)k_BT]$ is the Boltzmann factor, the tip angle is $\Theta = \omega_1 t_p$, where t_p is the pulse time, the transition frequency is denoted by ω_{pq}, and ξ_{pq} is the argument of $\langle p|\mathbf{I}\cdot\hat{n}|q\rangle$. The Rabi frequency is modified by

$$\lambda_{pq} \equiv |\langle p|\mathbf{I}\cdot\hat{n}|q\rangle|, \tag{12}$$

a unitless factor which will be referred to as the Rabi coefficient. In practice, when excitation is in the same direction as detection, Eq. (11) shows that the signal is proportional to $\lambda_{pq}\sin(\lambda_{pq}\Theta)$, and is therefore proportional to λ_{pq}^2 in the small-angle limit. The utility of the Rabi coefficient is that it contains all the geometric information of the effective excitation. Using Table II, the Rabi coefficients are a straightforward calculation. For the P-transitions, since I_+ and I_- are all zero, the Rabi coefficients are

$$\lambda_{12} = \sin\theta_\eta\cos\theta, \tag{13}$$

$$\lambda_{1'2'} = \sin\theta'_\eta\cos\theta. \tag{14}$$

Note that these are directly proportional to the EFG asymmetry and therefore the parallel transitions can be a direct metric of the EFG asymmetry. And for any O-transitions, they are

$$\lambda_{pq}^2 = \tfrac{1}{4}\sin^2\theta[\langle p|I_+|q\rangle^2 + \langle p|I_-|q\rangle^2 + 2\langle p|I_+|q\rangle\langle p|I_-|q\rangle\cos(2\varphi)]. \tag{15}$$

III. RESULTS

Here, results stemming from the theory in the previous section are presented. We first show a simulated spectrum produced from a specific EFG and magnetic field strength and elucidate how it relates to previous experimental ZNMR data on FeSCs. Several relationships are highlighted that can be used to understand such previously unanalyzed data. The analyzed data and comparisons to other experiments are summarized in Table III. Afterwards, we discuss the more general continuum of results, that is, for any arbitrary EFG and magnetic field strength. We also discuss the "observability" of the peaks, which will bring to light which parts of the continuum are easy or difficult to detect in an experiment. Lastly, we visualize the Rabi coefficients which are derived in Eqs. (13)–(15).

A. Predicted spectrum and Fe-based superconductors example

The spectrum is simulated using the quantities given in Table II and is shown in Fig. 3. This spectrum was generated by choosing specific R and θ_η values that closely resemble an experimental spectrum. All frequencies are normalized with respect to ω_+. The peak heights are calculated from the time-averaged, spatially averaged power of the signal. That is, if we take the signal to be $\langle\boldsymbol{\mu}\rangle_{pq}\cdot\hat{n}$, then the peak heights are given by

$$\left[\frac{1}{4\pi T}\int_S\int_0^T(\langle\boldsymbol{\mu}\rangle_{pq}\cdot\hat{n})^2\,dt\,d\Omega\right]^{1/2} \propto \sqrt{\langle p|I_+|q\rangle^2 + \langle p|I_-|q\rangle^2 + 2\langle p|I_z|q\rangle^2}, \tag{16}$$

where S is the spherical surface, T is the period, and Ω is the solid angle. [Note that this calculation neglects the Boltzmann factor and the sinusoidal dependence on the pulse strength shown in Eq. (11). For a powder, under optimal excitation, the result of this sinusoidal dependence would be of order unity in the final signal.] Finally, artificial broadening was applied to enhance visibility. The O/P-transitions, defined in Table II, are shown in the top/bottom panels and colored red/blue. In the figure, the O-transitions have been labeled by their first letters (e.g., ω_c corresponds to the "central" transition); the P-transitions are simply labeled by $\omega_\pm$.

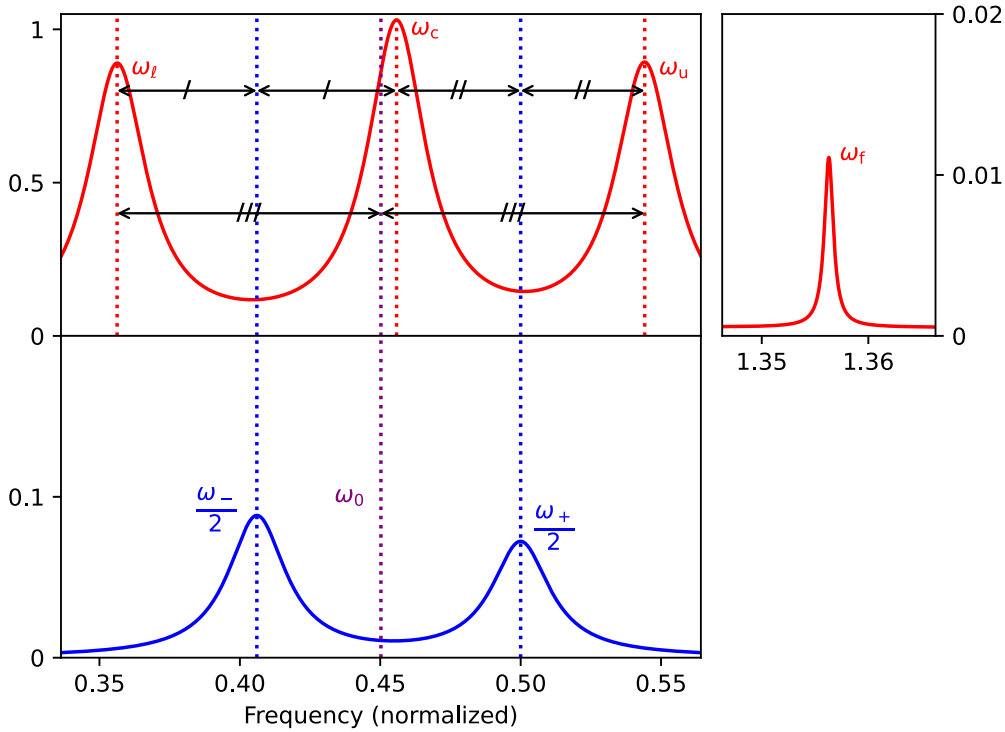

FIG. 3. A simulated spectrum of the combined Zeeman-quadrupolar Hamiltonian made with $R = 0.81$ and $\theta_\eta = 0.1$, showing all six possible transitions and the Zeeman frequency ω_0. All frequencies are normalized with respect to ω_+. The O-transitions are shown in red, and the P-transitions in blue, as defined in Table II. The frequencies of the P-transitions are placed at half of their actual value to aid in showing their relative positions with respect to the O-transitions. These relative positions of the frequencies are illustrated by the black arrow lines, hashed to denote equal spacing, and they are discussed in detail in Sec. III A. Peak widths were chosen arbitrarily.

The predicted spectrum in Fig. 3 was constructed to match that of particular FeSCs, which we have taken as a case study. FeSCs are characterized by their strong internal magnetic field, which results from the antiferromagnetic ordering of Fe magnetic moments. The magnetic ordering is an intrinsic feature of these materials, and therefore both the magnetic field and the EFG are fixed to the crystal structure. Since the crystal structure of these materials is either orthorhombic or tetragonal, depending on the phase, symmetry dictates that the internal magnetic field will always be aligned with one of the EFG principal axes. For these reasons, FeSCs can be studied by ZNMR using either a powder sample or a single crystal.

Several features in Fig. 3 can be discussed. First, the Zeeman frequency is simply the average of the lower and upper satellites. Second, from the formula for the central transition, it is clear that if there is no EFG asymmetry, then $\omega_c = \omega_0$ and the central transition would be exactly centered between the satellite peaks. Therefore, asymmetry of the central peak with respect to the satellite peaks is a clear indication of EFG asymmetry. Lastly, the quadrupole coupling constant can be determined by subtraction in quadrature of adjacent peak averages, that is, $(\omega_+^2 - \omega_-^2)/4 = 2\omega_0\omega_Q$. With regards to the P-transitions, it is more fruitful to discuss them in terms of half of their frequency values, which is how they are plotted in Fig. 3. This is because the average of the lower and central transitions is $\omega_-/2$. Similarly, the average of the central and upper transitions is $\omega_+/2$. Finally, the forbidden transition is the sum of the lower, central, and upper transitions, which is more evidently displayed in Fig. 2. With these relationships, one only needs to know three transitions in order to determine the other three. In particular, the simple relationship between the P and O transitions opens up the possibility of ready measurement, directly or indirectly, of the largely unexplored P-transitions.

The above analysis can be illustrated by examining two structurally similar FeSCs with very different spectra: $BaFe_2As_2$ [25] and $CaFe_2As_2$ [26], which represent all available ^{75}As ZNMR data with three peaks on FeSCs to date. Both of these materials were studied using a powder sample. We fit the existing experimental data, with equal weighting of the data points in the absence of publicly available error bars, as shown in Fig. 4. Using both the fits to determine the frequencies and the equations of ω_ℓ, ω_c, and ω_u found in Table II, we are able to solve for the quadrupole coupling constant, internal magnetic field, and EFG asymmetry parameter. These values are shown in Table III along with other literature values for comparison. The values in that table agree with some observations of Fig. 4. Namely, one can immediately see that the internal field of $CaFe_2As_2$ is nearly double that of $BaFe_2As_2$, as determined by the average of the satellite peaks shown as a dashed line in the figure. Further, the quadrupole coupling constant of $CaFe_2As_2$ is six times larger than that of $BaFe_2As_2$, as evidenced by the spread of the spectra around the central peak. The EFG asymmetry, which is indicated by the shift of the central peak from the Zeeman frequency, is clearly evident in $BaFe_2As_2$, but not in $CaFe_2As_2$. In fact, this shift can be estimated by considering the Taylor series expansion of ω_c around $|\omega_\perp|/(2\omega_0)$, which is small for both

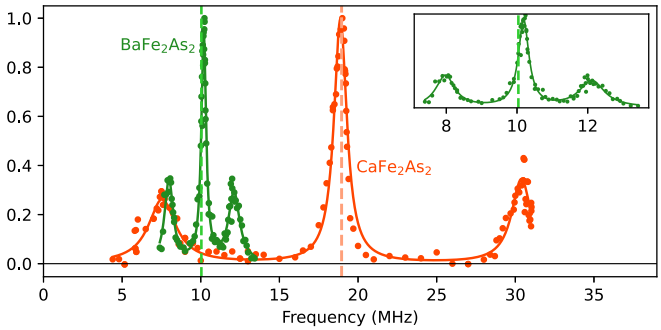

FIG. 4. The experimental spectra of $BaFe_2As_2$ [25] and $CaFe_2As_2$ [26], both performed at low temperature and at zero external field with powder samples. Data points were taken from the literature and fitted with three Lorentzian curves. The vertical dashed lines represent the Zeeman frequency for each system. These two systems are from the same family of FeSCs yet they represent two extremes of the EFG, indicated by central peak deviation from the Zeeman frequency, with $BaFe_2As_2$ having high EFG asymmetry and $CaFe_2As_2$ having zero EFG asymmetry. Larger EFG-quadrupolar coupling is indicated by a larger spread of the spectra. The quadrupole coupling constant, EFG asymmetry parameter, and internal field values are given in Table III.

materials. Doing so reveals that the central frequency shift $\Delta\omega_c = \omega_c - \omega_0$ can be approximated by

$$\Delta\omega_c \approx \frac{1}{12}\eta^2\frac{\omega_Q^2}{\omega_0}\left(1-\frac{\omega_Q^2}{4\omega_0^2}\right)^{-1}. \tag{17}$$

Note the shift is second order in η and always positive. The width of the vertical dashed lines in Fig. 4 indicates the uncertainty in the calculated ω_0 based on the lower and upper peaks. In this way, the clear shift (or lack thereof), including error, of the central peak away from ω_0 can easily be observed. Lastly, it should be noted that due to the small values of θ_η for these materials, the forbidden and P-transitions would be difficult to directly detect and, as expected, were not reported in the literature. In addition, η values were not reported perhaps due to the difficulty of extracting them without the use of analytic equations. Instead, we extracted those values by fitting the data reported in the literature, as described above.

In addition to the parameters we extracted, Table III also contains the same parameters, as quoted in the literature from high-field NMR experiments that used a single-crystal sample. Comparing between different methodologies for the same material, the quadrupole coupling constant and the internal field are in good agreement with each other. However, the EFG asymmetry parameter has notable disagreements for $CaFe_2As_2$, with ZNMR finding no EFG asymmetry but high-field NMR finding a sizable value of 0.39(5). It is unclear why this is the case, but it has been shown that the structure in this material is sensitive to different growth methodologies [32,33]. We suspect that depending on how the sample is grown, strain may exist that contributes to the EFG. In addition, the fit of data in Fig. 4 would yield different field values with nonuniform experimental error bars. The existence of such nonuniform error bars seems to be a real possibility, particularly considering the asymmetry in some of the peaks of Fig. 4. However, error bars, unfortunately, were not included in the literature. Further experimental work on these materials is needed to resolve discrepancies involving the EFG asymmetry.

B. Full solution observability

The two case studies in the previous section only represent two sets of (R, θ_η) values. Depending on the strength of the magnetic field and the EFG, spectra could be substantially different. Therefore, we show visualizations of the full solution set for the O-transitions in Fig. 5 and the P-transitions in Fig. 6. From these, one can quickly gain a sense of which Zeeman-quadrupolar strengths and EFG asymmetry give frequencies that can be observed and from which direction.

In the limit of small θ_η and $R \to 1$, which corresponds to high-field NMR, only three of the four O-transitions are observable: ω_u, ω_c, and ω_ℓ. Also, as expected, they are responsive only to circularly polarized magnetic fields, corotating with the standard rotating frame, with $\langle p|I_-|q\rangle \to 0$. The $\langle p|I_+|q\rangle$ ratio of the lower, central, and upper signals is found to be $\sqrt{3}{:}2{:}\sqrt{3}$, as has been found previously [3,34].

On the other hand, when $\omega_0 \to 0$, corresponding to the NQR limit, $\theta'_\eta = \pi - \theta_\eta$ and $R \to -1$ for finite ω_Q. In this limit, there is only one observable frequency, indicated by the equal values of ω_f, ω_c, and $\omega_\pm$, as expected. This is due to the double degeneracy of spin-3/2 nuclei in zero-field: $E_1 = E'_1$ and $E_2 = E'_2$. This creates two energy levels, each populated by nuclei with equal energies but mutually opposite spin states. A linearly polarized excitation will therefore excite both spin states, one for each circularly polarized component of the incident pulse. Hence the observed signal will also be linearly polarized, oscillating in the same direction as the excitation [35]. This is evident in the fact that ω_f and ω_c together have an equal but opposite response to the different helicity excitation; that is, $\langle 1|I_+|2'\rangle = -\langle 1'|I_-|2\rangle$ in this limit. Finally, since the signals of $\omega_\pm$ are inherently linear, we can conclude that the overall response is linear.

In the case of comparable Zeeman and quadrupolar strengths, $-1 < R < 1$. The observability of ω_u can be a metric of R, particularly for lower asymmetry with $\theta_\eta \leqslant \pi/4$, since it disappears as R becomes increasingly negative. It could be useful for tracking an appearing/disappearing internal magnetic field close to the phase transitions, in the case of FeSCs, for example. For general observability and tracking of dynamics, for instance T_1/T_2 data, the central line would be useful due to its strong responses for R not close to zero.

For the P-transitions plot shown in Fig. 6, only two rows are shown, corresponding to $\omega_\pm$. Since all frequencies are normalized with respect to ω_+, the frequency plot for the first P-transition, which is defined as ω_+, is seen as constant. The main features of observation are that for small values of θ_η and all values of R, the transitions would be difficult to observe directly. Observability increases with EFG asymmetry, and it may even serve as a metric of it as the Rabi coefficient is directly proportional to $\omega_\perp$.

C. Geometric dependence of the Rabi frequency

Finally, we examine the signal's dependence on the geometry of excitation and detection by visualizing the Rabi

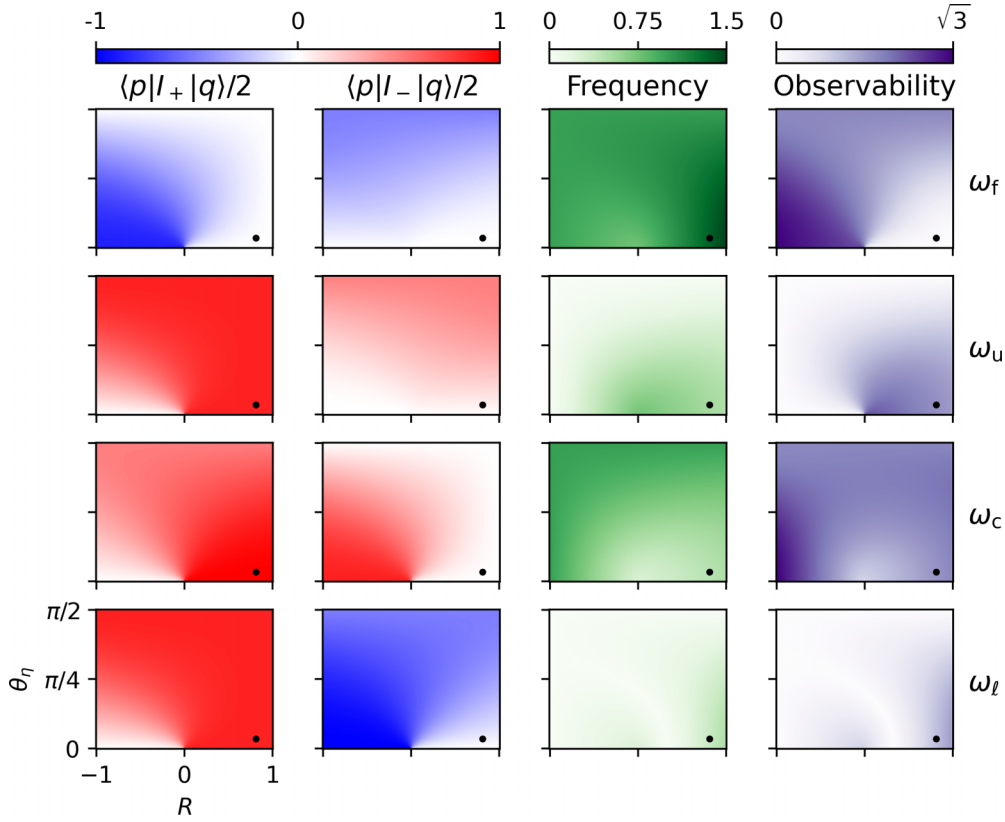

FIG. 5. Full solution of the Zeeman plus quadrupolar Hamiltonian spectrum for the O-transitions, as defined in Table II, as a function of R and θ_η. Each row corresponds to a different transition frequency, as labeled on the right side of the figure. Each column represents a different quantity of interest as labeled on the top of the figure. The first two columns are the matrix elements of the raising and lowering operators. Here, p and q refer to the labels of the eigenstates involved in the transition. The third column represents the actual transition frequency. Finally, the fourth column is the observability, which is calculated as $\omega_{pq}\sqrt{\langle p|I_+|q\rangle^2 + \langle p|I_-|q\rangle^2}$, where ω_{pq} is the transition frequency of the row. All frequency quantities are normalized with respect to ω_+. The black dots point to the R and θ_η values that generated Fig. 3.

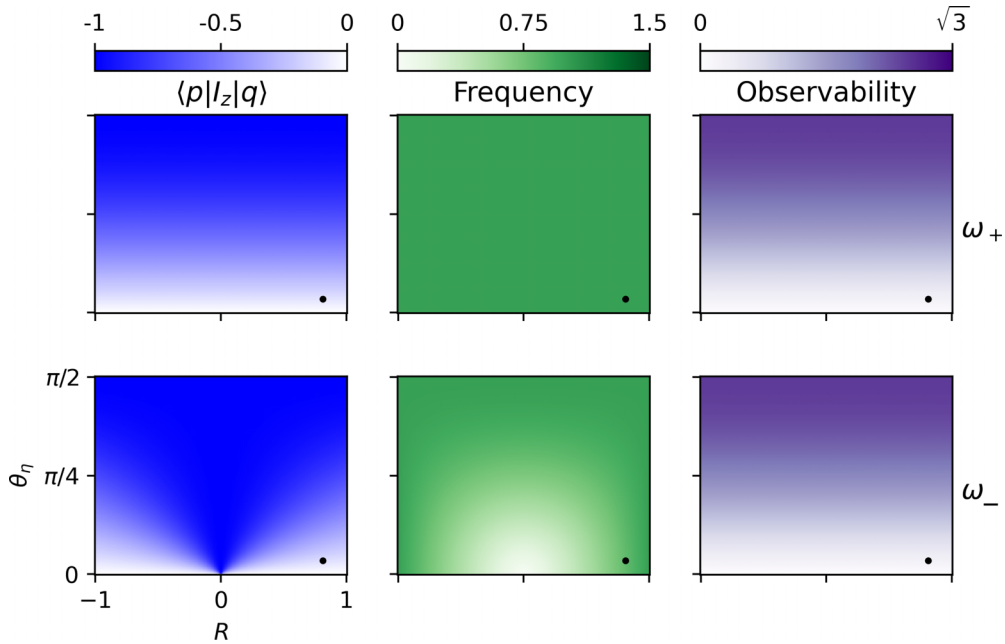

FIG. 6. Similar to Fig. 5, except the two rows correspond to the P-transitions, as defined in Table II. The observability is calculated by $\sqrt{2}\omega_{pq}|\langle p|I_z|q\rangle|$, where ω_{pq} is the transition frequency of the row. All frequency quantities are normalized with respect to ω_+. The black dots point to the R and θ_η values that generated Fig. 3.

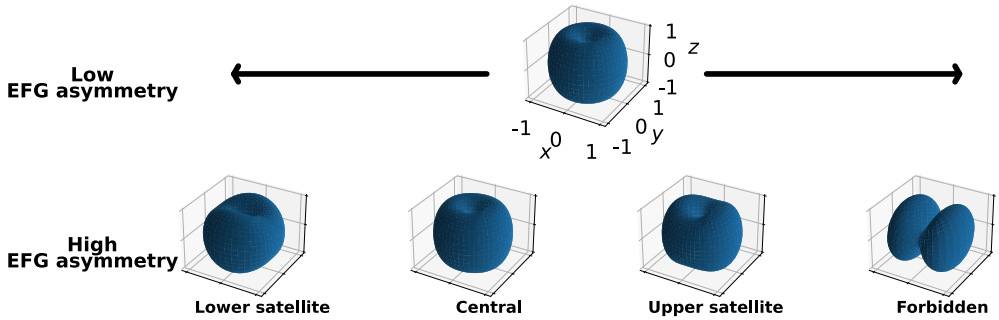

FIG. 7. Polar plots of the square of the Rabi coefficients λ^2, the geometric modifier of the Rabi frequency, for the O-transitions, as defined in Eq. (15). These plots allow for a simple geometric representation of the observed signal, relative to the magnetic field which is oriented along z. A particular value of $R = 0.81$ is chosen for all plots, but with $\theta_\eta = 0.1$ for high EFG asymmetry (bottom row) and $\theta_\eta = 0.001$ for low EFG asymmetry (top row). Each column corresponds to a different O-transition, as labeled below each column. For the low EFG asymmetry row, all plots look nearly identical, hence only one plot is shown. All values have been normalized with respect to the maximum of each subplot.

coefficient, as defined in Eq. (12). Assuming the use of a single crystal, we can use this coefficient to gain a better understanding of how the signal will behave for different geometric orientations. In particular, we are focused on signals such that excitation and detection are along the same direction with linear polarization.

Starting with the four O-transitions, their Rabi coefficients are given by Eq. (15). In particular, we plot λ^2_{pq} in 3D real space, as shown in Fig. 7. Due to the cyclic nature of the spin angular momentum operators in θ_η and θ'_η, defined in Table II, all of the features of the plots can be reproduced by some phase shift. Namely, all of the Rabi coefficient plots are phase-shifted from the central transition plots in the following ways: a $\theta'_\eta - \pi$ phase shift for the lower satellite, a $\theta_\eta + \pi$ phase shift for the upper satellite, and both a $\theta'_\eta - \pi$ and $\theta_\eta + \pi$ phase shift for the forbidden transition. For that reason, only the unique features of the plots are shown in the figure. For example, for high EFG asymmetry values, the signal can be highly asymmetric for some of the O-transitions. In contrast, for low EFG asymmetry, the O-transitions are all highly symmetric about the z-axis. In all four plots, however, the concept of the O-transition, that is, transitions that are unaffected by excitations parallel to the magnetic field, is captured with obvious dips right on the z-axis.

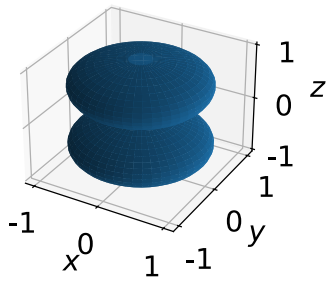

FIG. 8. This is also a plot of the square of the Rabi coefficient, similar to Fig. 7, except for the P-transitions, defined in Eqs. (13) and (14). Only one transition is shown, and for a single pair of (R, θ_η) because the features of the plot are identical for all values. As expected, no signal is seen orthogonal to the z direction, which is parallel to the magnetic field.

For the two P-transitions, the Rabi coefficients are shown in Fig. 8. Only one plot is shown because both plots, when normalized, have identical features for all values of R and θ_η. The plots are symmetric about z, with the values collapsing to zero on the $x-y$ plane. This is sensible since the P-transitions are insensitive to excitations orthogonal to the magnetic field. This could be potentially useful with regard to materials with internal magnetic fields, such as the FeSCs. In this context, in theory with a single crystal, the geometry of the static magnetic field and the EFG could be determined with just the transition frequencies that are detected. For example, if the P-transitions are detected, then some component of the static magnetic field lies along $\mathbf{B}_1$. If they are not detected, the field is orthogonal to $\mathbf{B}_1$.

IV. CONCLUSIONS

In this paper, the spectrum from the combined Zeeman and quadrupole Hamiltonian of spin-3/2 particles is calculated for the case in which the magnetic field is aligned with one of the EFG principal axes. We derive succinct closed-form solutions for transition frequencies. In addition, we derive the magnetic moment arising from resonant excitation as a function of excitation strength and direction as well as explicit expressions for the Rabi coefficients, given in Eqs. (13)–(15). The results can be used not only for conventional NMR, where the magnetic field is applied externally, but also for systems that produce static internal magnetic fields.

An important example of materials with intrinsic fields can be found in FeSCs. Pre-existing ^{75}As spectra from two such materials are analyzed. Because both the magnetic and EFG fields are intrinsic to the crystal's structure, these spectra, arising from powder samples, are not broadened. Therefore, the field values obtained compare well to single-crystal goniometer measurements done with conventional NMR. For these materials, three of the six possible transitions dominate. With analytic expressions, the spectra are readily interpreted—the average of the satellite frequencies is the Zeeman frequency, subtraction in quadrature of adjacent peak averages is proportional to the quadrupole coupling constant, and the deviation of the central peak from the Zeeman frequency can be used to calculate the EFG asymmetry. While the first two calculations are straightforward, the latter is more involved. Therefore, the

relative uncertainty on the asymmetry parameter is larger than on the other two field quantities.

In contrast, the Rabi coefficient of the P-transitions is found to be directly proportional to the EFG asymmetry parameter. This dependency can potentially be exploited to characterize the asymmetry. For instance, excitation on one of the P-transitions will alter the populations of the corresponding energy levels shown in Fig. 2, according to the strength of the associated Rabi coefficient. The resulting population changes in the quantum levels can then be read out on the more readily detectable O-transitions. Although the P-transitions are often weak, they are easily found once the three dominant O-transitions are known, since the P-transitions are themselves related to the frequencies of the O-transitions by averages, as shown in Fig. 3. There is precedence for such two-frequency schemes in other systems [36–38]. Such indirect detection of the asymmetry parameter could be sensitive and therefore particularly useful for studying systems with small asymmetry. An interesting example is the use of asymmetry as a metric for spin-fluctuations in FeSCs [16].

In conclusion, the exact predictions presented here provide a firm foundation for future research with spin-3/2 particles immersed in a magnetic field aligned with the EFG frame.

ACKNOWLEDGMENTS

We would like to thank Shinji Kawasaki for insightful conversations and for supplying his data to us for analysis. In addition, we would like to thank Igor Mazin and Nick Curro for their input. This work was supported by the National Science Foundation (Award No. 2214194) and the Quantum Science & Engineering Center at George Mason University.

[1] G. Muha, Exact solution of the eigenvalue problem for a spin 3/2 system in the presence of a magnetic field, J. Magn. Reson. (1969) **53**, 85 (1983).

[2] R. Creel and D. Drabold, Exact analytic solution of the spin 3/2 combined Zeeman-quadrupole Hamiltonian, J. Mol. Struct. **111**, 85 (1983).

[3] A. D. Bain, Exact calculation, using angular momentum, of combined Zeeman and quadrupolar interactions in NMR, Mol. Phys. **101**, 3163 (2003).

[4] A. D. Bain, Quadrupole interactions: NMR, NQR, and in between from a single viewpoint, Magn. Reson. Chem. **55**, 198 (2017).

[5] A. D. Bain, The NMR of quadrupolar nuclei. relationship between exact and perturbation solutions for spin 3/2, Chem. Phys. Lett. **531**, 267 (2012).

[6] C. Dean, Zeeman splitting of nuclear quadrupole resonances, Phys. Rev. **96**, 1053 (1954).

[7] F. A. Perras, C. M. Widdifield, and D. L. Bryce, QUEST—QUadrupolar Exact SofTware: A fast graphical program for the exact simulation of NMR and NQR spectra for quadrupolar nuclei, Solid State Nucl. Magn. Reson. **45**, 36 (2012).

[8] D. Possa, A. C. Gaudio, and J. C. Freitas, Numerical simulation of NQR/NMR: Applications in quantum computing, J. Magn. Reson. **209**, 250 (2011).

[9] C. Odin, Calculations of multipulse sequence in NQR of spins 3/2, J. Magn. Reson. **141**, 239 (1999).

[10] N. Sinjavsky, M. Ostafin, and M. Maćkowiak, Determination of the asymmetry parameter of EFG tensor from moments of NQR nutation spectra in powders, Appl. Magn. Reson. **15**, 215 (1998).

[11] G. S. Harbison, A. Slokenbergs, and T. M. Barbara, Two-dimensional zero-field nutation nuclear quadrupole resonance spectroscopy, J. Chem. Phys. **90**, 5292 (1989).

[12] T. Leigh Spencer, G. R. Goward, and A. D. Bain, Complete description of the interactions of a quadrupolar nucleus with a radiofrequency field. implications for data fitting, Solid State Nucl. Magn. Reson. **53**, 20 (2013).

[13] T. L. Spencer, G. R. Goward, and A. D. Bain, Exact calculation of the response of a quadrupolar nucleus to radio frequency irradiation, Can. J. Chem. **89**, 764 (2011).

[14] I. I. Mazin, Superconductivity gets an iron boost, Nature (London) **464**, 183 (2010).

[15] P. Carretta and G. Prando, Iron-based superconductors: tales from the nuclei, Riv. Nuovo Cimento **43**, 1 (2020).

[16] J. N. Ansari, K. L. Sauer, and I. I. Mazin, Slow tail of nematic spin fluctuations in $Ba(Fe_{1-x}Co_x)_2As_2$: Insight from nuclear magnetic resonance, Phys. Rev. B **108**, 064516 (2023).

[17] H. Yasuoka, T. Shimizu, T. Imai, S. Sasaki, Y. Ueda, and K. Kosuge, NMR and NQR studies in high-T_c oxides: $YBa_2Cu_3O_y (6.0 \leqslant y \leqslant 6.91)$, Hyperfine Interact. **49**, 167 (1989).

[18] A. Lombardi, M. Mali, J. Roos, D. Brinkmann, and I. Mangelschots, Temperature dependence of the sublattice magnetization of the antiferromagnet $Ca_{0.85}Sr_{0.15}CuO_2$, Phys. Rev. B **54**, 93 (1996).

[19] E. A. Donley, J. L. Long, T. C. Liebisch, E. R. Hodby, T. A. Fisher, and J. Kitching, Nuclear quadrupole resonances in compact vapor cells: The crossover between the NMR and the nuclear quadrupole resonance interaction regimes, Phys. Rev. A **79**, 013420 (2009).

[20] A. Narath, Antiferromagnetism in $CoCl_2 \cdot 2H_2O$. II. chlorine nuclear magnetic resonance and paramagnetic susceptibility, Phys. Rev. **140**, A552 (1965).

[21] D. Bennett, D. Miljak, and J. Khachan, The measurement of chalcopyrite content in rocks and slurries using magnetic resonance, Miner. Eng. **22**, 821 (2009).

[22] C. P. Slichter, *Principles of Magnetic Resonance* (Springer, Berlin, 1990).

[23] C. Cohen-Tannoudji, B. Diu, and F. Laloë, *Quantum Mechanics. Volume 1: Basic Concepts, Tools, and Applications*, 2nd ed. (Wiley-VCH Verlag, Weinheim, 2020).

[24] H. R. Brooker and R. B. Creel, Zeeman nuclear quadrupole resonance line shapes in powders ($I = 3/2$), J. Chem. Phys. **61**, 3658 (1974).

[25] H. Fukazawa, K. Hirayama, K. Kondo, T. Yamazaki, Y. Kohori, N. Takeshita, K. Miyazawa, H. Kito, H. Eisaki, and A. Iyo, ^{75}As NMR study of the ternary iron arsenide $BaFe_2As_2$, J. Phys. Soc. Jpn. **77**, 093706 (2008).

[26] S. Kawasaki, T. Oka, T. Tabuchi, X. Wang, X. Chen, and G. qing Zheng, As-NMR/NQR study of pressure-induced superconductivity in $CaFe_2As_2$, J. Phys. Chem. Solids **72**, 501 (2011).

[27] S.-H. Baek, N. J. Curro, T. Klimczuk, E. D. Bauer, F. Ronning, and J. D. Thompson, First-order magnetic transition in single-crystalline $CaFe_2As_2$ detected by ^{75}As nuclear magnetic resonance, Phys. Rev. B **79**, 052504 (2009).

[28] A. P. Dioguardi, J. Crocker, A. C. Shockley, N. ApRoberts Warren, C. Lin, K. R. Shirer, D. Nisson, A. Lodhia, P. Klavins, and N. J. Curro, Angular dependent ^{75}As NMR study of the electric field gradient in $CaFe_2As_2$, Supercond. Sci. Technol. **26**, 025012 (2013).

[29] N. J. Curro, A. P. Dioguardi, N. ApRoberts-Warren, A. C. Shockley, and P. Klavins, Low-energy spin dynamics in the antiferromagnetic phase of $CaFe_2As_2$, New J. Phys. **11**, 075004 (2009).

[30] J. Cui, B. Roy, M. A. Tanatar, S. Ran, S. L. Bud'ko, R. Prozorov, P. C. Canfield, and Y. Furukawa, Antiferromagnetic spin correlations and pseudogaplike behavior in $Ca(Fe_{1-x}Co_x)_2As_2$ studied by ^{75}As nuclear magnetic resonance and anisotropic resistivity, Phys. Rev. B **92**, 184504 (2015).

[31] K. Kitagawa, N. Katayama, K. Ohgushi, M. Yoshida, and M. Takigawa, Commensurate itinerant antiferromagnetism in $BaFe_2As_2$: ^{75}As-NMR studies on a self-flux grown single crystal, J. Phys. Soc. Jpn. **77**, 114709 (2008).

[32] B. Saparov, C. Cantoni, M. Pan, T. C. Hogan, W. Ratcliff, 2nd, S. D. Wilson, K. Fritsch, B. D. Gaulin, A. S. Sefat, and M. Tachibana, Complex structures of different $CaFe_2As_2$ samples, Sci. Rep. **4**, 4120 (2014).

[33] Y. Furukawa, B. Roy, S. Ran, S. L. Bud'ko, and P. C. Canfield, Suppression of electron correlations in the collapsed tetragonal phase of $CaFe_2As_2$ under ambient pressure demonstrated by ^{75}As NMR/NQR measurements, Phys. Rev. B **89**, 121109(R) (2014).

[34] A. J. Ramsay and A. Rossi, Relaxation dynamics of spin-3/2 silicon vacancies in 4*h*-SiC, Phys. Rev. B **101**, 165307 (2020).

[35] M. J. Weber and E. L. Hahn, Selective spin excitation and relaxation in nuclear quadrupole resonance, Phys. Rev. **120**, 365 (1960).

[36] V. Grechishkin, V. Anferov, and N. J. Sinjavsky, Adiabatic demagnetization and two-frequency methods in ^{14}N quadrupole resonance spectroscopy, in *Advances in Nuclear Quadrupole Resonance* (Wiley, London, 1983), Vol. 5, pp. 13–23.

[37] G. V. Mozjoukhine, The two-frequency nuclear quadrupole resonance for explosives detection, Appl. Magn. Reson. **18**, 527 (2000).

[38] K. Sauer, B. Suits, A. Garroway, and J. Miller, Three-frequency nuclear quadrupole resonance of spin-1 nuclei, Chem. Phys. Lett. **342**, 362 (2001).